Time-Resolved Areal-Density Measurements with Proton Spectroscopy in Spherical Implosions

The goal of the inertial confinement fusion (ICF)[1,2] implosion is to achieve high-enough temperature and compression of the fuel to sustain thermonuclear burn. The burn begins with spark ignition of the central hot spot[2] that is created as a result of shock heating and target compression. The burn wave then propagates into the higher-density regions of the compressed shell, releasing energy through the products of thermonuclear reactions.[2] The combination of high temperature and high density–radius product (called areal density or ρR) of the compressed target is necessary to ignite the target and achieve high gain.[1] In the direct-drive ignition target design[3] for the National Ignition Facility (NIF),[2] a 3.4-mm-diam, 350-μm-thick cryogenic deuterium–tritium (DT) shell is imploded with 192 overlapped laser beams with a total energy of 1.5 MJ. The hot-spot areal density must be ~300 mg/cm^2 at a temperature exceeding ~10 keV to ignite. The expected neutron yield of 2.5×10^{19} (corresponding to a gain of ~45) will be achieved at a fuel temperature of ~30 keV and a target areal density of ~1200 mg/cm^2 at peak compression. Areal densities measured so far in cryogenic implosions[4–7] are far below the values necessary for ignition because far-lower laser energy is used and the unstable growth of target perturbations inhibits achieving the desired compression. In recent implosions on the 60-beam, 351-nm OMEGA laser system, areal densities of ~40 mg/cm^2 have been achieved with cryogenic D_2 targets and laser energies of ~23 kJ.[7]

Because of the technical complexity associated with cryogenic equipment, most ICF implosions use plastic or glass shells filled with different gases, allowing a large variety of diagnostics to be used in experiments. Indirect-drive implosions on the Nova laser achieved ~15 mg/cm^2 of gas and ~70 mg/cm^2 of shell areal densities, respectively.[8] Recent studies on OMEGA reported up to ~15 mg/cm^2 of gas and ~60 mg/cm^2 of shell areal densities measured with charged-particle diagnostics.[9] Measurements using shell absorption of x rays emitted from the hot core reported[10] shell areal densities up to ~100 mg/cm^2. The highest reported values of areal densities, up to ~1 g/cm^2, are from implosions on the GEKKO XII laser system.[11]

To date, all reported values of target compression are time averaged over the neutron and charged-particle production. During this time, the target areal density is expected to grow by an order of magnitude or more. Time-integrated particle spectra (used to measure average areal densities) clearly show signatures of time evolution. For example, in OMEGA experiments with 24-μm-thick shells filled with 18 atm of D^3He gas, primary proton spectra have two distinctive features from shock and compression phases of implosion.[12] These features are produced when target areal densities differ by a factor of ~10, with a corresponding time difference of ~500 ps. This article describes experiments where the measured neutron production histories combined with primary 14.7-MeV proton spectra of D^3He fuel allows the first determination of areal-density *growth* during the time of neutron production up to peak compression. These measurements become possible when all other aspects contributing to the shape of the proton spectrum, such as geometrical broadening from the finite size of the proton-production region, broadening from small-scale target nonuniformities, and ion temperature broadening, are taken into account. In this article we not only present for the first time target-areal-density evolution, a fundamental quantity for ICF, but also provide areal-density growth measurements for the study of unstable growth of target perturbations, an area of the utmost importance to the success of ICF.

The experiment consisted of two direct-drive implosions on the 60-beam OMEGA laser system.[13] The targets were ~950-μm-initial-diam, 20-μm-thick plastic CH shells filled with 18 atm (shot 25220) and 4 atm (shot 25219) of D^3He gas. Neutron-production histories from the reaction $D + D \rightarrow {}^3He(0.82\ MeV) + n\ (2.45\ MeV)$ were measured with the neutron temporal diagnostic (NTD).[14] Proton spectra from the reaction $D + {}^3He \rightarrow {}^4He(3.6\ MeV) + p(14.7\ MeV)$ have been measured with seven wedged-range filters (WRF's)[15] to ensure approximately uniform coverage of the target. The shapes of the time-integrated proton spectra depend primarily on the evolution of the target areal density and the temporal history of proton production (which is approximately proportional to the measured neutron-production history). Implo-

sions of targets with an equivalent mass of D_2 and DT fuels provide values of neutron yield and ion temperature (measured using scintillator detectors), neutron burn width (using the neutron bang-time detector),[14] and average fuel areal density (from detection of knock-on deuterons),[9] which together are used to estimate sizes of particle production and fuel regions at peak neutron production. These sizes are required to determine the extent of geometrical and temperature broadening contributions to the shapes of proton spectra. Results from equivalent implosions with shells having titanium-doped layers provide measurements of areal-density modulations (by means of differential imaging),[16] which also contribute to the widths of the proton spectra. The targets were imploded with a 1-ns square pulse with a total on-target energy of ~23 kJ. All laser beams were smoothed with distributed phase plates,[17] 1-THz, two-dimensional smoothing by spectral dispersion,[18] and polarization smoothing[19] using birefringent wedges. The average beam-to-beam energy imbalance was about 3% to 4%.

Figure 91.40 shows the results of a simulation of shot 21240, which had a 12-atm-D^3He fill, performed with the 1-D hydrocode *LILAC*;[20] these results were used to develop and test a fitting method to determine the areal-density evolution. Protons born in nuclear reactions [Fig. 91.40(a)] are slowed down by the plasma of the gas fuel and plastic shell [the simulated areal-density evolution is shown by a solid curve in Fig. 91.40(b)] on the way out from the target core to the detector. The energies of protons leaving the target are calculated using the Bethe–Bloch stopping power[21] relation, which depends very weakly on the plasma density and temperature. The slowing-down curve shown in Fig. 91.40(c) has been calculated for a fully ionized CH plasma with an electron density of 10^{25} cm^{-3} (corresponding to plastic density of ~35 g/cm^3) and a temperature of 0.5 keV. The proton spectrum [Fig. 91.40(d), solid line] represents the integral of the protons born and slowed down by the target. The resulting proton spectrum is additionally broadened by the core ion temperature of 3.4 keV and geometrical effects, discussed below.

The areal-density evolution is inferred by fitting a constructed spectrum $P_c(E)$ to the measured $P_m(E)$ proton spectrum. The spectrum $P_c(E)$ is constructed using the measured neutron-production rate (assumed to be proportional to the proton-production rate) and the target areal density ρR_t, assumed to have a Lorentzian form as a function of time t:

$$\rho R_t(t) = C_0 \Big/ \left[(t - C_1)^2 + (C_2/2)^2 \right].$$

The best fit is achieved using a χ^2 minimization of the deviation between $P_c(E)$ and $P_m(E)$ by varying three fitting parameters C_0, C_1, and C_2. The sensitivity and systematic errors of

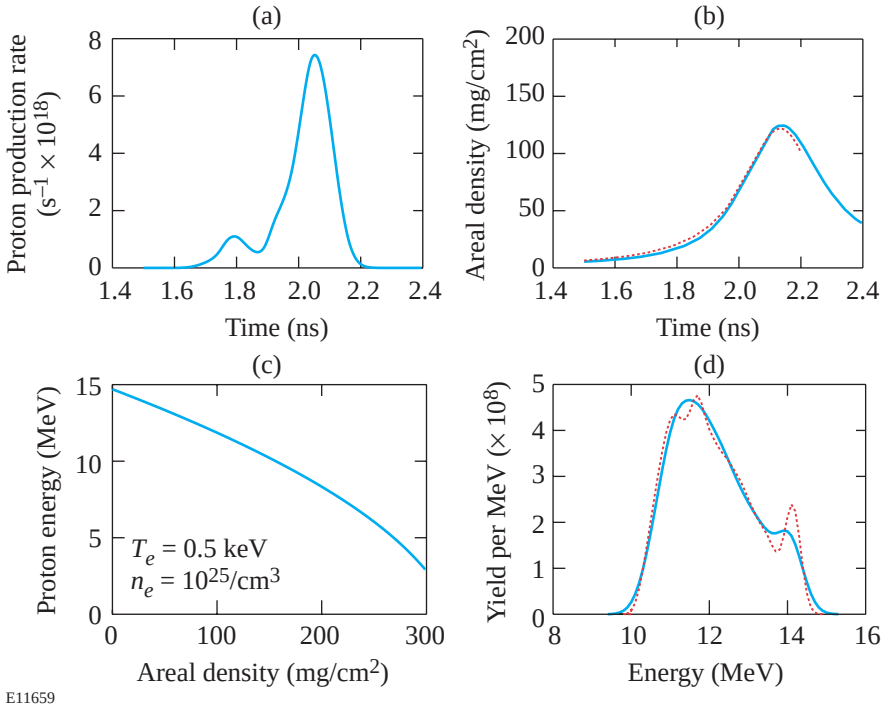

E11659

Figure 91.40
The results of 1-D *LILAC* simulations (solid lines) and the calculated fit (dashed lines) for shot 21240: (a) the proton-production history; (b) the target-areal-density evolution; (c) the proton energy versus target areal density calculated using Bethe–Bloch stopping power for an electron density of 10^{25}/cm^3 and a temperature of 0.5 keV; and (d) the proton energy spectra.

this method have been tested with the simulation results shown in Fig. 91.40 by comparing the fit with the simulated areal-density evolution. The dashed lines in Figs. 91.40(b) and 91.40(d) show that a good fit for the yield is achieved when the fitted areal-density evolution is very close to the actual. This method is very sensitive because even small (10% at ~100 mg/cm^2) variations in areal density result in sizable deviations (~0.5 MeV) in the proton spectrum. The fitting assumes that the ion temperature, size of the core, shell, production region, and stopping power do not change in time. The uncertainties of these approximations are included in the systematic errors discussed below.

Geometrical broadening effects are described schematically in Fig. 91.41(a), and the resulting broadening shapes are shown in Fig. 91.41(b). In these calculations the gas fuel occupies a spherical region of radius R_2 and a proton-production region of radius R_1. On the way to the distant detector, protons lose their energy primarily in the shell of thickness R_3–R_2. Protons that are born on the x axis (which passes through the core center and the detector) always leave the target in a direction normal to the shell, while protons that are born off this axis penetrate the shell at some angle to the shell normal. As a result, even for an undistorted shell, the protons reaching the detector will have an energy spectrum broader than that originally emitted from the production region since the amount of proton energy loss depends on the path length in the shell. Figure 91.41(b) shows spectra of monoenergetic protons after passing a uniform shell of various areal densities for a target with $R_1 = 27\ \mu$m, $R_2 = 33\ \mu$m, and $R_3 = 63\ \mu$m, taken from the *LILAC* simulation presented in Fig. 91.40. The number of protons reaching the detector in the x direction as a function of coordinate z ($0 \le z \le R_1$) have the distribution

$$F(z) = Cz\sqrt{R_1^2 - z^2}\,,$$

where C is a constant derived using the target geometry shown in Fig. 91.41(a). The effective areal density seen by the protons going to the detector as a function of z is

$$\rho R_{\text{eff}}(z) = \rho\left(\sqrt{R_3^2 - z^2} - \sqrt{R_2^2 - z^2}\right).$$

Substituting z for ρR_{eff} in the expression for $F(z)$ and converting areal density to proton energy using Fig. 91.40(c) results in the geometrically broadened shapes shown in Fig. 91.41(b). The original monoenergetic proton spectrum shifts to lower proton energies and broadens as a result of geometrical effects. For each shot, the parameters R_1, R_2, and R_3 have been calculated using experimental results from a large number of shots with fills having an equivalent mass of D_2 and DT. For example, in implosions with 15-atm-D_2 fuel (mass equivalent to 18 atm of D^3He), R_2 = 36 μm has been calculated using conservation of fuel mass (8.3×10^{-7} g) and measured fuel areal density (~15 mg/cm^2). In order to match the experimental neutron yield of ~1.6×10^{11}, the particle-production volume must have $R_1 = 22\ \mu$m with a measured ion temperature of ~3.7 keV and a neutron burn width of ~170 ps. In an implosion with 3-atm-D_2 fuel (mass equivalent to 4 atm of D^3He), radii of $R_1 = 25\ \mu$m and $R_2 = 32\ \mu$m were calculated based on the fuel mass of 1.67×10^{-7} g, fuel areal density of ~4 mg/cm^2, neutron yield of ~6.6×10^{10}, ion temperature of ~5 keV, and neutron burn width of ~150 ps. The shell thickness R_3–R_2, the most-insensitive parameter on fitting results, has been taken to be 30 μm for both types of implosions.

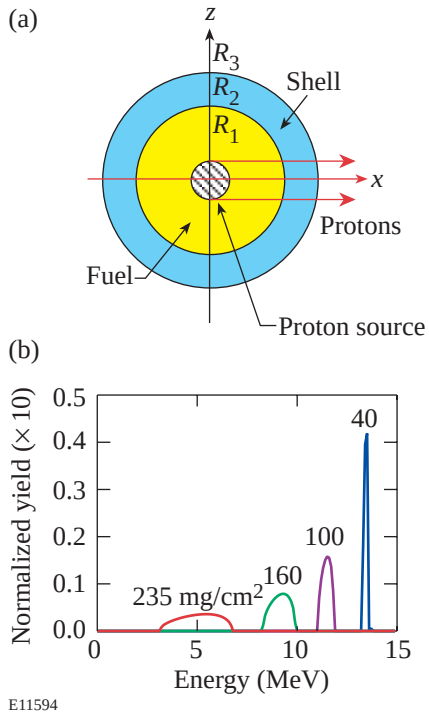

Figure 91.41
The geometrical broadening effects. Panel (a) shows the target schematic. The proton-production region has a radius of R_1, the gas fuel has a radius of R_2, and the shell has a thickness of R_3–R_2. The protons travel to a distant detector in the direction of the x axis. Panel (b) shows the geometrically broadened shapes, as normalized 14.7-MeV proton spectra after passing through shells with areal densities of 40, 100, 160, and 235 mg/cm^2, calculated for R_1 = 27 μm, R_2 = 33 μm, and R_3 = 63 μm.

Figure 91.42 shows the proton spectrum fitting results for shot 25220 with 18 atm of D^3He gas for seven detectors, which provided approximately uniform coverage of the shell. Inferred areal-density time histories for all seven directions are shown by the solid lines in Fig. 91.42(h) together with the neutron-production history (dotted line). The additional small effect of short-scale (with mode number $\ell > 6$) areal-density nonuniformities on proton spectrum broadening has been corrected by reducing the areal density shown in Fig. 91.42 by 7% with the uncertainty ranging from 0% to 15% included in the error bars: Differential imaging measurements[16] of inner-shell, titanium-doped layers show areal-density perturbation levels of ~15% at peak neutron production. In the whole shell these values are about ~7%, as calculated by 2-D simulations,[16] because the whole shell is more uniform than the inner layer, which is unstable during the deceleration phase of the implosion. The constant correction due to this effect is a good approximation (even though the measured shell modulations grow throughout the implosion) since its contribution to spectral broadening is maximum at peak neutron production and lower at peak compression because of lower amount of protons contributing to it. In experiments, ~70% of total proton spectrum width is due to the areal-density evolution, ~20% is due to geometrical effects, and the remaining ~10% is due to temperature, short-scale (with mode number $\ell > 6$) areal-density perturbations, and instrumental broadening. A discussion of the experimental error analysis is presented in Appendix A.

Figure 91.43 summarizes the results for shots with (a) 18-atm- and (b) 4-atm-D^3He fills and compares them with 1-D *LILAC* predictions. The more-stable 18-atm-fill shot has a measured peak areal density of 109±14 mg/cm^2 (thick solid line), which is close to the 1-D simulation result (thin solid line); however, the more-unstable 4-atm shot has a measured peak areal density of 123±16 mg/cm^2, much lower than the 1-D simulation result of 230 mg/cm^2. During neutron production (from 1.6 to 2.0 ns), the areal density grows by a factor of ~8 in the 4-atm shot. At peak compression, the areal-density asymmetries with low mode numbers $\ell \le 6$ are ~10% and ~20% for 18-atm- and 4-atm-fill targets, respectively, as estimated from the measured values in the seven detectors. The measured peak areal density is only about 10% higher for the 4-atm-fill target than that of the 18-atm-fill target. This is consistent with core sizes of R_2 = 32 μm and 36 μm, respectively, estimated using neutron and particle measurements.

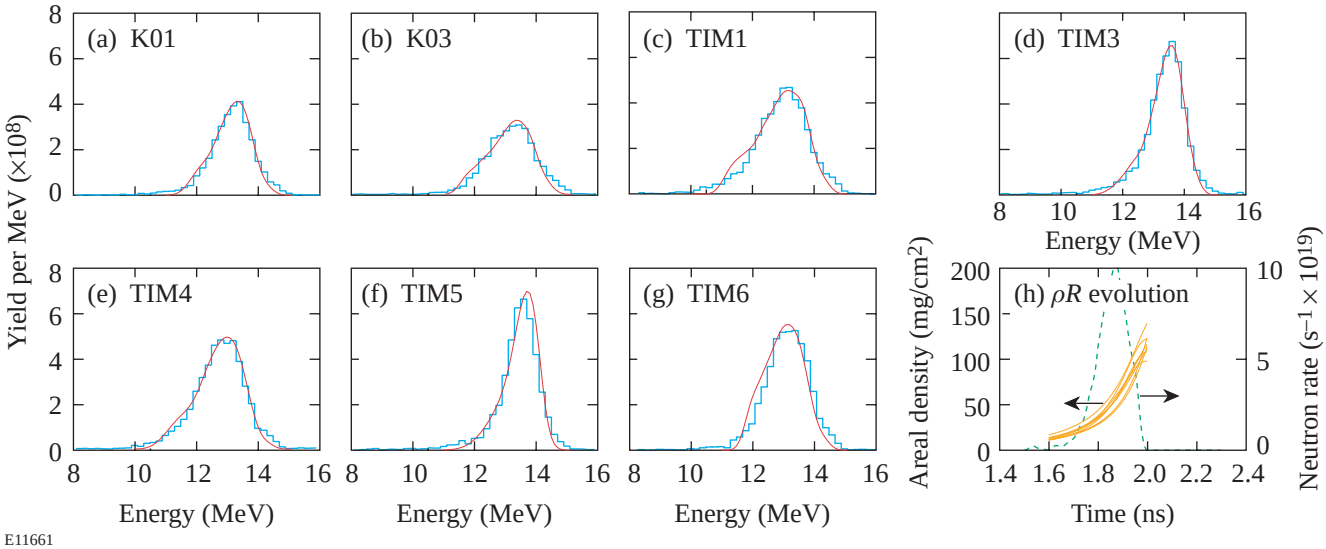

Figure 91.42
The proton spectra and fitting results (smooth solid lines) for shot 25220 with 18 atm of D^3He gas [(a)–(g)]. (h) Also shown is the inferred areal-density evolution in seven directions (solid lines) and the neutron-production history (dotted line) for this shot.

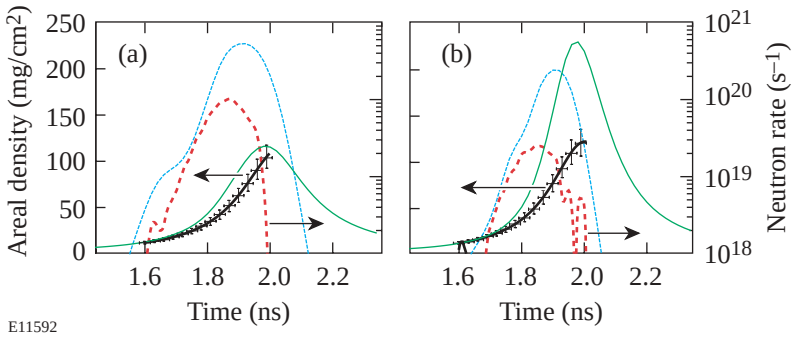

Figure 91.43
The measured (thick) and simulated (thin) target areal-density evolutions (solid) and neutron-production histories (dashed) for shots with (a) 18-atm and (b) 4-atm gas fills.

In conclusion, the target areal density grows by a factor of ~8 during the time of neutron production (~400 ps) before reaching 123±16 mg/cm^2 at peak compression in the shot with a 20-μm-thick plastic CH target filled with 4 atm of D^{3}He fuel. This value is lower by a factor of ~2 than the 1-D simulation result of 230 mg/cm^2. For the more-stable, 18-atm-fill target, the target areal density reaches 109±14 mg/cm^2 at peak compression, close to the 1-D prediction of 115 mg/cm^2.

ACKNOWLEDGMENT

This work was supported by the U.S. Department of Energy Office of Inertial Confinement Fusion under Cooperative Agreement No. DE-FC03-92SF19460, the University of Rochester, and the New York State Energy Research and Development Authority. The support of DOE does not constitute an endorsement by DOE of the views expressed in this article.

Appendix A

The errors in the areal-density evolution measurements include systematic errors calculated from the sensitivity analysis of the fitting results and statistical errors of measured proton spectra. The biggest systematic error is the uncertainty in plasma conditions that affect proton stopping power. The relevant error is about ±0.5 MeV at a proton energy of 10 MeV, which translates to an areal-density uncertainty of ±10% at 100 mg/cm^2. The use of neutron instead of proton-production history resulted in a 24-ps temporal shift of the areal-density evolution. The assumption that the proton-production size R_1 is constant during proton production gives an uncertainty of ±0.3 MeV at 10 MeV, which translates to an areal-density uncertainty of ±6% at 100 mg/cm^2. The uncertainty in the other geometrical parameters R_2 and R_3 are negligibly small in the present analysis. The additional uncertainty due to possible ion-temperature evolution is also calculated to be negligible compared to other errors. The statistical errors due to the noise in the proton spectra, neutron-production history, and the errors in the fitting parameters C_0, C_1, and C_2 have been estimated to be ±0.5 MeV at 10 MeV, which translates to an areal-density uncertainty of ±10% at 100 mg/cm^2. Averaging over seven independent measurements makes them even smaller.

REFERENCES

1. J. Nuckolls *et al.*, Nature **239**, 139 (1972).
2. J. D. Lindl, Phys. Plasmas **2**, 3933 (1995).
3. P. W. McKenty, V. N. Goncharov, R. P. J. Town, S. Skupsky, R. Betti, and R. L. McCrory, Phys. Plasmas **8**, 2315 (2001).
4. R. R. Johnson *et al.*, Phys. Rev. A **41**, 1058 (1990).
5. F. J. Marshall, S. A. Letzring, C. P. Verdon, S. Skupsky, R. L. Keck, J. P. Knauer, R. L. Kremens, D. K. Bradley, T. Kessler, J. Delettrez, H. Kim, J. M. Soures, and R. L. McCrory, Phys. Rev. A **40**, 2547 (1989).
6. K. A. Tanaka *et al.*, Phys. Plasmas **2**, 2495 (1995).
7. C. Stoeckl, C. Chiritescu, J. A. Delettrez, R. Epstein, V. Yu. Glebov, D. R. Harding, R. L. Keck, S. J. Loucks, L. D. Lund, R. L. McCrory, P. W. McKenty, F. J. Marshall, D. D. Meyerhofer, S. F. B. Morse, S. P. Regan, P. B. Radha, S. Roberts, T. C. Sangster, W. Seka, S. Skupsky, V. A. Smalyuk, C. Sorce, J. M. Soures, R. P. J. Town, J. A. Frenje, C. K. Li, R. D. Petrasso, F. H. Séguin, K. Fletcher, S. Padalino, C. Freeman, N. Izumi, R. Lerche, and T. W. Phillips, Phys. Plasmas **9**, 2195 (2002).
8. M. D. Cable *et al.*, Phys. Rev. Lett. **73**, 2316 (1994).
9. C. K. Li, F. H. Séguin, D. G. Hicks, J. A. Frenje, K. M. Green, S. Kurebayashi, R. D. Petrasso, D. D. Meyerhofer, J. M. Soures, V. Yu. Glebov, R. L. Keck, P. B. Radha, S. Roberts, W. Seka, S. Skupsky, C. Stoeckl, and T. C. Sangster, Phys. Plasmas **8**, 4902 (2001).
10. F. J. Marshall, J. A. Delettrez, V. Yu. Glebov, R. P. J. Town, B. Yaakobi, R. L. Kremens, and M. Cable, Phys. Plasmas **7**, 1006 (2000).
11. H. Azechi *et al.*, Laser Part. Beams **9**, 193 (1991).
12. R. D. Petrasso, F. H. Séguin, J. A. Frenje, C. K. Li, J. R. Rygg, B. E. Schwartz, S. Kurebayashi, P. B. Radha, C. Stoeckl, J. M. Soures, J. Delettrez, V. Yu. Glebov, D. D. Meyerhofer, and T. C. Sangster, "Measuring Implosion Dynamics through ρR Evolution in Inertial Confinement Fusion Experiments," submitted to Phys. Rev. Lett.

13. T. R. Boehly, D. L. Brown, R. S. Craxton, R. L. Keck, J. P. Knauer, J. H. Kelly, T. J. Kessler, S. A. Kumpan, S. J. Loucks, S. A. Letzring, F. J. Marshall, R. L. McCrory, S. F. B. Morse, W. Seka, J. M. Soures, and C. P. Verdon, Opt. Commun. **133**, 495 (1997).

14. R. A. Lerche, D. W. Phillion, and G. L. Tietbohl, Rev. Sci. Instrum. **66**, 933 (1995).

15. F. H. Séguin, C. K. Li, D. G. Hicks, J. A. Frenje, K. M. Green, R. D. Petrasso, J. M. Soures, D. D. Meyerhofer, V. Yu. Glebov, C. Stoeckl, P. B. Radha, S. Roberts, C. Sorce, T. C. Sangster, M. D. Cable, S. Padalino, and K. Fletcher, Phys. Plasmas **9**, 2725 (2002).

16. V. A. Smalyuk, J. A. Delettrez, V. N. Goncharov, F. J. Marshall, D. D. Meyerhofer, S. P. Regan, T. C. Sangster, R. P. J. Town, and B. Yaakobi, Phys. Plasmas **9**, 2738 (2002).

17. Y. Lin, T. J. Kessler, and G. N. Lawrence, Opt. Lett. **20**, 764 (1995).

18. S. P. Regan, J. A. Marozas, J. H. Kelly, T. R. Boehly, W. R. Donaldson, P. A. Jaanimagi, R. L. Keck, T. J. Kessler, D. D. Meyerhofer, W. Seka, S. Skupsky, and V. A. Smalyuk, J. Opt. Soc. Am. B **17**, 1483 (2000).

19. T. R. Boehly, V. A. Smalyuk, D. D. Meyerhofer, J. P. Knauer, D. K. Bradley, R. S. Craxton, M. J. Guardalben, S. Skupsky, and T. J. Kessler, J. Appl. Phys. **85**, 3444 (1999).

20. J. Delettrez, R. Epstein, M. C. Richardson, P. A. Jaanimagi, and B. L. Henke, Phys. Rev. A **36**, 3926 (1987).

21. T. A. Mehlhorn, J. Appl. Phys. **52**, 6522 (1981).